Local nanoscale strain mapping of a metallic glass during in situ testing

Christoph Gammer, Colin Ophus, Thomas C. Pekin, Jürgen Eckert, and Andrew M. Minor

Citation: Appl. Phys. Lett. **112**, 171905 (2018); doi: 10.1063/1.5025686
View online: https://doi.org/10.1063/1.5025686
View Table of Contents: http://aip.scitation.org/toc/apl/112/17
Published by the American Institute of Physics

Local nanoscale strain mapping of a metallic glass during *in situ* testing

Christoph Gammer,[1,a)] Colin Ophus,[2] Thomas C. Pekin,[2,3] Jürgen Eckert,[1,4] and Andrew M. Minor[2,3]

[1]*Erich Schmid Institute of Materials Science, Austrian Academy of Sciences, Jahnstraße 12, 8700 Leoben, Austria*
[2]*National Center for Electron Microscopy, Molecular Foundry, Lawrence Berkeley National Laboratory, 1 Cyclotron Road, Berkeley, California 94720, USA*
[3]*Department of Materials Science and Engineering, University of California, Berkeley, California 94720, USA*
[4]*Department Materials Physics, Montanuniversität Leoben, Jahnstraße 12, 8700 Leoben, Austria*

(Received 12 February 2018; accepted 6 April 2018; published online 26 April 2018)

The local elastic strains during tensile deformation in a CuZrAlAg metallic glass are obtained by fitting an elliptic shape function to the characteristic amorphous ring in electron diffraction patterns. Scanning nanobeam electron diffraction enables strain mapping with a resolution of a few nanometers. Here, a fast direct electron detector is used to acquire the diffraction patterns at a sufficient speed to map the local transient strain during continuous tensile loading *in situ* in the transmission electron microscope. The elastic strain in tensile direction was found to increase during loading. After catastrophic fracture, a residual elastic strain that relaxes over time was observed. *Published by AIP Publishing.* https://doi.org/10.1063/1.5025686

Local elastic strains can strongly modify the properties of crystalline materials, for example, mechanical strength,[1,2] electronic band structure,[3] optical properties,[4] the critical irradiation dose for crystalline-to-amorphous phase transitions,[5] and many others. Therefore, for many experiments, it is important to accurately measure the local strain distribution with as high spatial resolution as possible. Scanning/transmission electron microscopy (S/TEM) is often used to measure the local strain due to its high accuracy and spatial resolution.[6–9] In particular, STEM nanobeam electron diffraction (NBED) has emerged as a particularly useful technique for measuring local strains,[10–13] due in large part to the widespread use of high speed direct electron detectors.[14–16] In the case of amorphous materials, X-ray diffraction is frequently used to map the strain distributions.[17] Residual strains and stresses have been observed in deformed metallic glasses (MGs) and are a promising route for enhancing their ductility.[18,19] Less work has focused on mapping the local strains in amorphous materials with TEM. Recently, strain mapping with selected area electron diffraction was demonstrated,[20] with fairly limited resolution. In this study, we use scanning NBED to measure the local strain at the nanoscale during an *in situ* nanomechanical tensile test to fully demonstrate the capability of visualizing the distribution of elastic strains inside an amorphous material using electron microscopy.

To demonstrate *in situ* strain mapping of amorphous materials, we deformed a CuZr-based MG in tension. $Cu_{36}Zr_{48}Al_8Ag_8$ ingots were prepared by arc melting of high-purity elements. From the ingots, rods (3 mm in diameter) were cast into Cu-molds by suction-casting (modified Bühler MAM1 device). From the MG, electrotransparent TEM specimens were prepared by electropolishing. To achieve a tensile specimen with minimal damage, a FIB-SEM (FEI Strata 235) was used to cut a rectangle from the electron transparent region of the sample and transfer it to a Hysitron Push-to-Pull device using an Omniprobe micromanipulator.[21] The Push-to-Pull Device transforms the compressive motion of the indenter into a well-defined *in situ* tensile test in the TEM. The sample was attached using a Pt-deposition system and cut into a miniaturized dogbone with a width of 250 nm, a length of 850 nm, and a thickness of 190 nm. Deformation was carried out using a Hysitron PI95 Picoindenter under displacement control.

Figure 1 shows the experimental setup used in this study. The dog-bone shaped MG specimen is deformed *in situ* in the TEM. To image the specimen, a slightly converged electron beam is scanned over the sample and an annular dark-field (ADF) image is recorded in STEM mode. In addition, a full NBED pattern is recorded for every probe position using a fast electron detector. A beamstop is used to prevent damage to the detector from the unscattered electron beam. STEM diffraction mapping was carried out using a FEI Titan operated at 300 kV. A Gatan K2 IS direct electron detector is used that is capable of recording diffraction patterns with a resolution of 1920×1792 pixels, at a frame rate of 400 f/s. The speed of the detector enables recording a NBED map with a size of 128×64 probe positions in ≈20 s. The resulting 4D dataset consisting of thousands of diffraction patterns contains a vast amount of information. Using arbitrary virtual apertures, images can be computed from NBED maps without facing the limitations of a monolithic STEM detector.[22,23] In addition, the radial distribution function can be computed from each diffraction pattern to map the local structure.[24]

Here, we demonstrate that the dataset can be used to compute strain maps during deformation even in an amorphous material. The diffraction pattern of an amorphous material is characterized by a diffuse ring pattern. The first ring can be used to determine the strain, as it induces a small deviation from an ideal circle.[17,25] The position of the first ring as a function of scattering angle, $q(\theta)$, is compared to

a)christoph.gammer@oeaw.ac.at

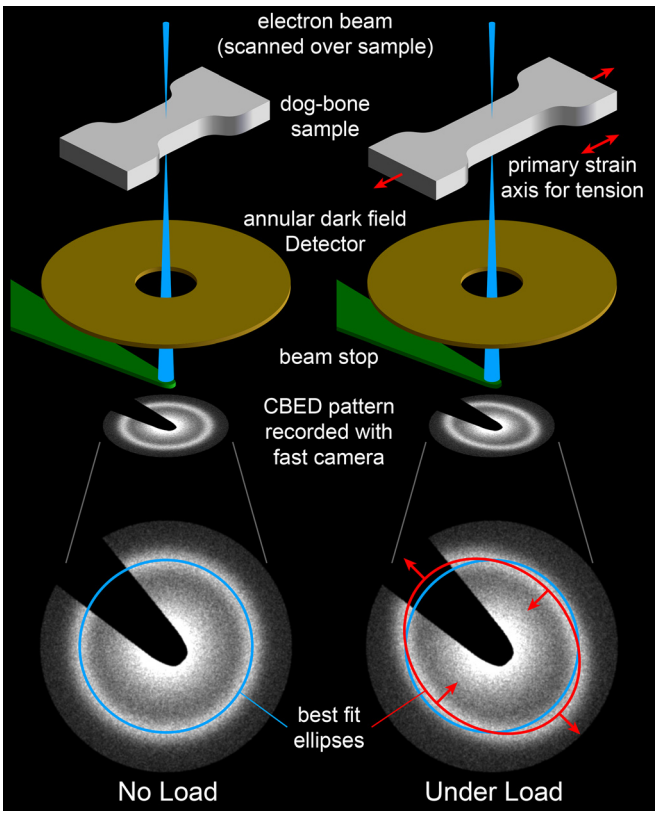

FIG. 1. Experimental geometry used in this study. A dog-bone shaped metallic glass sample is deformed *in situ* in the scanning electron microscope. The sample is placed at the cross-over position of the convergent electron beam. The convergent electron beam diffracts from the sample, leading to the characteristic amorphous ring pattern. A best fit ellipse is computed for each diffraction image recorded at each probe position. The elastic strain induced during loading leads to an elliptic distortion of the amorphous ring pattern.

the radius of the ideal ring of the unstrained case, q_0. The resulting strain, ϵ, a function of θ, can be separated into the axial, tangential, and shear strains ϵ_{xx}, ϵ_{yy}, and ϵ_{xy}.

$$\epsilon(\theta) = \frac{q_0 - q(\theta)}{q(\theta)} = \epsilon_{xx}\cos^2(\theta) + \epsilon_{xy}\cos(\theta)\sin(\theta) + \epsilon_{yy}\sin^2(\theta).$$

This equation can be rewritten as

$$\frac{q_0}{q(\theta)} = 1 + \epsilon_{xx}\cos^2(\theta) + \epsilon_{xy}\cos(\theta)\sin(\theta) + \epsilon_{yy}\sin^2(\theta). \quad (1)$$

In the present work, we have determined the strain by analyzing the ellipticity of the NBED patterns. Each diffraction pattern of the CuZr-based MG sample has a characteristic amorphous ring at a scattering angle of $q_0 = 4.2\,\mathrm{nm}^{-1}$. To determine the ellipticity, we have fitted the ring intensity $I(q_x, q_y)$ over the reciprocal space coordinates (q_x, q_y) using the following form:

$$I(q) = I_r \exp\left[-\frac{\left(q_0 - \sqrt{Aq_x^2 + Bq_xq_y + Cq_y^2}\right)^2}{2s^2}\right] + I_0 + I_1\sqrt{q_x^2 + q_y^2}, \quad (2)$$

where I_r, I_0, and I_1 are the intensities of the ring, constant background, and linear background, respectively. A, B, and C are the ellipse coefficients, and s is the standard deviation of the ring, equivalent to its width. Note that the coordinate system (q_x, q_y) is centered on the middle of the diffraction pattern. This position varies by several pixels over the full set of probe positions and must therefore be included as a fitting parameter. After an initial fit of all the diffraction patterns including the center as fitting parameters, we set the center coordinate to be the best-fit plane over all probe positions. The shift is caused by an instrumental limitation in the shift-tilt purity and it might alternatively be corrected for by performing a sample-free scan. After setting the center coordinate, we performed a second fit of all the diffraction patterns.

Once Eq. (2) has been fitted to all probe positions, the strain can be computed from the results for A, B, and C. A and C will be very close to a value of 1 and B close to 0. Therefore, we define $A = 1 + a$ and $C = 1 + c$. Converting the ellipse to polar coordinates $(q_x = q(\theta)\cos(\theta),\ q_y = q(\theta)\sin(\theta))$ yields

$$q(\theta)^2((1+a)\cos^2(\theta) + B\cos(\theta)\sin(\theta) + (1+c)\sin^2(\theta)) = q_0^2,$$
$$\frac{q_0}{q(\theta)} = \sqrt{1 + a\cos^2(\theta) + B\cos(\theta)\sin(\theta) + c\sin^2(\theta)}.$$

This expression can be approximated, by taking into account that a, B, and c are small

$$\frac{q_0}{q(\theta)} \approx 1 + \frac{1}{2}(a\cos^2(\theta) + B\cos(\theta)\sin(\theta) + c\sin^2(\theta)).$$

A comparison of this equation with Eq. (1) allows deducing the strain

$$\epsilon_{xx} \approx \frac{1}{2}(A-1), \quad \epsilon_{xy} \approx \frac{1}{2}B, \quad \epsilon_{yy} \approx \frac{1}{2}(C-1). \quad (3)$$

By determining the ellipticity for each diffraction pattern in the NBED map, a full two-dimensional strain map is obtained. When the MG specimen is deformed *in situ* in the TEM, the local elastic strain changes, resulting in a change in the elliptic distortion (see Fig. 1). By obtaining a time series of NBED maps, time resolved strain maps can be calculated and the change in the local strain during deformation can be mapped *in situ*. Note that all real experiments will contain some elliptic distortion even for non-strained samples, due to aberrations in the projector lenses of the microscope. Therefore, a reference has to be defined and the distortions measured in this region are used as reference values. We have used the measured ellipticity of the MG specimen prior to deformation as the reference strain state.

Figure 2 show the results from the three NBED maps recorded during continuous *in situ* deformation. The MG specimen was loaded at a rate of 0.3 nm/s under displacement control. Figures 3(a)–3(c) give the ADF-STEM images recorded during deformation. Figures 3(a) and 3(b) show the specimen during loading and Fig. 3(c) after catastrophic fracture. The corresponding strain maps obtained from the NBED maps are given in Fig. 2. The initial loading is given in Figs. 2(a)–2(e). Figure 2(a) shows the mean diffraction pattern computed from all NBED patterns along with the best fit ellipse. To increase

the precision for the strain measurement, the camera length was selected to show only the first ring. In Fig. 2(b), a virtual dark-field image is shown that was computed by summing the intensity in the first ring for each NBED pattern. The coordinate system was chosen with the x-axis in tensile direction and the y-axis normal to it and transferred to the diffraction pattern taking the image rotations of the microscope into account [see Figs. 2(a) and 2(b)]. Figures 2(c)–2(e) show the strain maps calculated from the elliptic distortions of the NBED patterns using Eq. (2). The strain was determined for each of the 8192 individual NBED patterns. The strain in tensile direction (ϵ_{xx}), the strain normal to the tensile direction (ϵ_{yy}), and the shear strain (ϵ_{xy}) are shown. It is important to note that continuous loading is carried out during NBED mapping. Therefore, there is a strain difference within each panel, due to the extended duration of the scan. The elongation of the specimen increases as the electron beam scans from top to bottom of the map. Therefore, the strain in tensile direction ϵ_{xx} as well as the compressive strain normal to the tensile direction ϵ_{yy} increase slightly from top to bottom of the map during continued loading [see Figs. 2(c) and 2(d)]. The shear strain ϵ_{xy} remains close to zero.

Figures 2(f)–2(j) show the strain maps computed from the second scan during continued loading of the specimen. The mean diffraction pattern shows no obvious differences to the initial state. However, under closer inspection, a small change in elliptic distortion becomes apparent. The comparison of the mean ellipse before and during loading is shown in Fig. 2(f) in blue and red, respectively. The virtual dark-field in Fig. 2(g) shows a slight elongation of the tensile bar. The corresponding strain maps are shown in Figs. 2(h)–2(j). Again, it should be noted that NBED mapping is carried out during continuous loading, i.e. the top of the map corresponds to less deformation than the bottom of the map. Therefore, an increase in the tensile strain (ϵ_{xx}) from top to bottom of the map can be observed within the tensile bar. Similarly, ϵ_{yy} shows an increase in compressive strain. The shear strain ϵ_{xy} on the other hand remains zero. Only a small amount of shear strain at the shoulders of the tensile bar can be observed [see Fig. 2(j)], demonstrating the well-defined tensile loading conditions. At the end of the second frame, the MG sample fractures abruptly. It should be pointed out that due to the continuous loading, the strain during fracture is higher than the strain values shown in Figs. 2(h)–2(j). The results from the third frame, acquired after fracture, are shown in Figs. 2(k)–2(o). The MG tensile bar fractures along a single sharp fracture plane. The thinner areas caused by the inclined fracture plane result in a contrast change in the virtual dark-field [see Fig. 2(l)] and the ADF-STEM image [see Fig. 3(c)]. The sudden release of the external load after fracture induces a significant change in the elliptic distortion as shown in the mean NBED pattern [see Fig. 2(k)]. The strain maps calculated from the elliptic distortions of all NBED patterns is given in Figs. 2(m)–2(o). Both ϵ_{xx} and ϵ_{yy} are significantly reduced due to the release of the external strain; however, residual elastic strain remains.

Figure 3(d) shows the time evolution of the local elastic strain. The specimen is scanned row by row during NBED strain mapping. Therefore, the strain maps can be converted into time resolved strain values, by plotting each strain value in the map against the time when the NBED pattern was recorded. For a better statistics, the mean value across the tensile bar is computed yielding one value for each row of the scan. In addition, the standard deviation is computed [see Fig. 3(e)]. It has to be pointed out that in this analysis, the time resolved strain values stem from different regions from

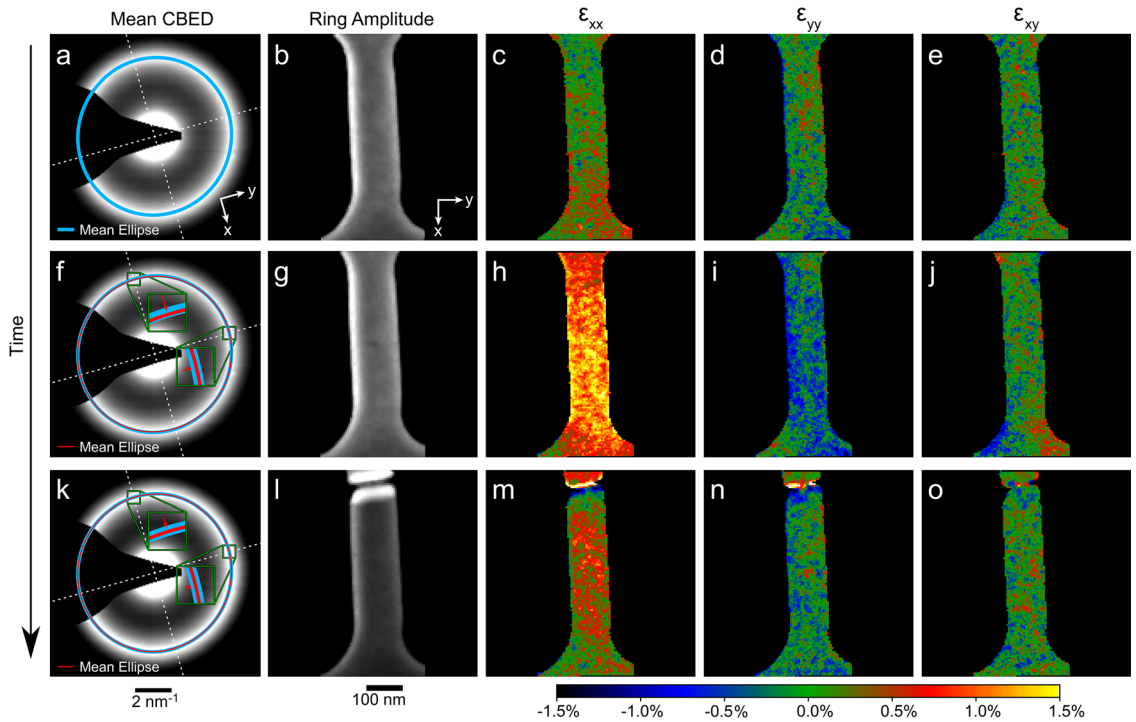

FIG. 2. Results from the nanodiffraction maps obtained during *in situ* deformation. The average diffraction pattern and a virtual dark-field image are shown along with the color-coded strain maps. Three time resolved maps are shown. The sample is deformed under continuous loading (a)–(e) and (f)–(j) before showing catastrophic fracture (k)–(o).

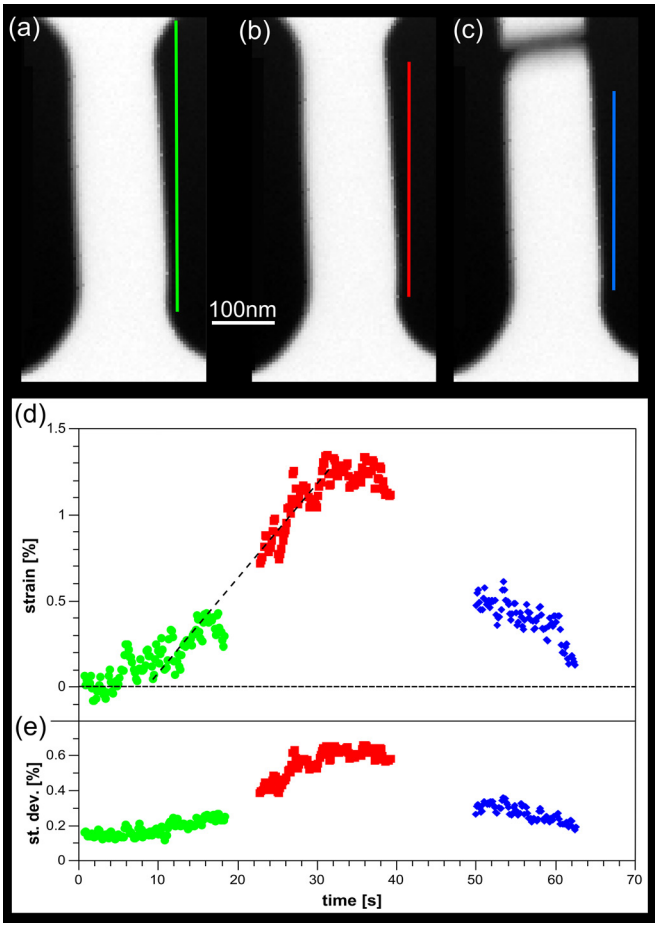

FIG. 3. Time evolution of the strain in tensile direction. The mean value across the tensile bar is computed yielding one value for each row in the scan. (a)–(c) The rows used for the analysis are indicated in the three scans. (d) During continued loading, the strain increases and decreases after fracture. The dashed line serves as guide to the eye. (e) In addition, the standard deviation is computed indicating significant strain inhomogeneities.

the tensile bar. Therefore, an assumption is made about uniform deformation across the entire sample, which can be assumed for MG specimens during elastic deformation.

This analysis is carried out for all three scans. Only the gauge section is used in the analysis. The regions used are indicated with lines in Figs. 3(a)–3(c). The green data points in Fig. 3(d) show the values for ϵ_{xx} obtained from the first scan. Initially, prior to loading, they scatter around zero. Upon continuous loading, ϵ_{xx} increases. During continued loading, the strain values further increase [red dots in Fig. 3(d)]. The dashed line serves as a guide to the eye. It should be pointed out that the current data does not represent a stress strain curve. Still, the deviation from the linear elastic regime before fracture is an indication for plastic deformation that is expected to occur in miniaturized MG specimens.[26] After fracture, ϵ_{xx} drops significantly to around 0.5% but does not fully recover [blue dots in Fig. 3(d)]. The time evolution of ϵ_{xx} indicates that the residual strain relaxes with time. The standard deviation of the local elastic strain, $st.dev._{\epsilon xx}$, is plotted as a function of time in Fig. 3(e). The results demonstrate that the standard deviation increases upon tensile loading. Significant strain inhomogeneities in ϵ_{xx} that increase with loading can be seen in Fig. 3. The increase indicates that in addition to the standard deviation stemming from the accuracy of the method, there are structural strain inhomogeneities that become more pronounced with loading.

The increase in structural strain inhomogeneities happens during elastic loading, indicating that nanoscale heterogeneities in the specimen have differing responses to stress.[27] From the quantitative values of ϵ_{xx} and ϵ_{yy}, we can directly determine the Poisson's ratio $\nu = -\frac{\epsilon_{yy}}{\epsilon_{xx}}$, yielding a value of around 0.33 for the present experiment. This value is in accordance with the values measured for bulk CuZr-based MGs (around 0.36).[28] Similar measurements of the Poisson's ratio were carried out from the elastic strains measured during *in situ* deformation of amorphous TiAl $\nu = 0.23$.[20] The Poisson's ratio is an important parameter as it is linked to the ductility of the MG and can deviate based on composition and structure of the materials.[27] The method presented here allows for the direct local measurement of ν in the specimen during deformation. Deformation experiments of small scale MG samples have shown a larger elastic strain limit and a residual plastic strain in the specimen after deformation.[26,29] In specimens of similar size, the residual plastic strain measured from the gauge length is around 0.8%.[29] Here, we use the elliptic distortion to measure ϵ_{xx} locally and observe significant residual elastic strain after fracture ($\epsilon_{xx} \sim 0.4\%$). The residual elastic strain relaxes with time in the unloaded sample indicating that local rearrangements after deformation result in a decrease in elastic strain. In elastostatically loaded specimens, residual strains were observed after unloading.[30] Similarly, plastic deformation can induce residual strains.[31,32] Frequently, these strain distributions are inhomogeneous, yielding MG "composites" with soft and hard areas that show an increased ductility.[18,19]

Different approaches have been proposed for measuring the ellipticity in electron diffraction patterns of nanocrystalline and amorphous materials.[20,33] Integration of sectors offers high speed and good precision, but works best for data with a high signal to noise ratio. On the other hand, direct fitting of a ring to the first diffuse ring shows a high precision and works for a lower signal to noise ratio. Typically, the starting values are very close to the resulting best fit mean ellipse, due to the small changes in ellipticity and mean intensity throughout the diffraction patterns, allowing to reduce the time needed for the fit. The precision for the strain determined from electron diffraction patterns can reach 0.01% for selected area electron diffraction patterns.[20] The present data give a strain precision of around 0.1%. This value can be improved by boosting the signal-to-noise ratio through the use of an energy filter or an increase in the sample volume. X-ray diffraction is routinely used to map the strain in MG specimens; however, the resolution is limited due to the large volume sampled for each diffraction pattern. In the case of electron diffraction, the strong interaction of electrons with matter allows to map strain at the nanoscale, thus opening up an experimentally unexplored length-scale. Quantitative data for the transient elastic strain field during deformation in MGs on the nanoscale enable direct comparison with shear strains observed in MD simulations. The resolution and sensitivity of *in situ* NBED mapping has the potential to experimentally reveal local deformation events[34] and directly link them to the local structure. This is of great importance, as the lack of long-range order in MGs hindered direct imaging of fundamental deformation mechanisms so far.

In conclusion, we have determined the local atomic-level elastic strains in a MG specimen by fitting an ellipse to the first diffuse ring in the electron diffraction pattern. By using a fast electron detector, the presented method can be combined with *in situ* TEM deformation to determine the local transient nanoscale strain. We applied the method to a CuZrAlAg MG specimen deformed in tension. Time resolved strain maps with a spatial resolution of 7 nm were recorded during continuous loading, without pausing the experiment. The results show an increase in the elastic strain during loading. A residual elastic strain is observed after fracture that relaxes over time. The present experiment demonstrates the feasibility of nanoscale *in situ* strain mapping in MG specimens. The demonstrated setup allows to record time-resolved strain maps with a spatial resolution down to 1 nm by combining NBD mapping with a fast electron detector. The experimental measurement of local quantitative strain enables greater insight into the deformation processes in MGs on the nanoscale and the potential for direct comparison with atomistic simulations on similar size scales.

We would like to thank D. Beitelschmidt for providing the MG specimens. The authors acknowledge support of the European Research Council under the ERC Advanced Grant INTELHYB (Grant No. ERC-2013-ADG-340025). T.P. and A.M. were supported by the Director, Office of Science, Office of Basic Energy Sciences, Materials Sciences and Engineering Division, of the U.S. Department of Energy under Contract No. DE-AC02-05-CH11231 within the Mechanical Behavior of Materials program. Work at the Molecular Foundry was supported by the Office of Science, Office of Basic Energy Sciences, of the U.S. Department of Energy under Contract No. DE-AC02-05CH11231.

[1]G. T. Hahn and A. R. Rosenfield, "Metallurgical factors affecting fracture toughness of aluminum alloys," Metall. Mater. Trans. A **6**, 653–668 (1975).
[2]Z. Li, K. G. Pradeep, Y. Deng, D. Raabe, and C. C. Tasan, "Metastable high-entropy dual-phase alloys overcome the strength–ductility trade-off," Nature **534**, 227–230 (2016).
[3]P. R. Chidambaram, C. Bowen, S. Chakravarthi, C. Machala, and R. Wise, "Fundamentals of silicon material properties for successful exploitation of strain engineering in modern CMOS manufacturing," IEEE Trans. Electron Devices **53**, 944–964 (2006).
[4]J. Quereda, P. San-Jose, V. Parente, L. Vaquero-Garzon, A. J. Molina-Mendoza, N. Agraït, G. Rubio-Bollinger, F. Guinea, R. Roldán, and A. Castellanos-Gomez, "Strong modulation of optical properties in black phosphorus through strain-engineered rippling," Nano Lett. **16**, 2931–2937 (2016).
[5]W. Guo, T. Iwashita, and T. Egami, "Universal local strain in solid-state amorphization: The atomic size effect in binary alloys," Acta Mater. **68**, 229–237 (2014).
[6]R. Bierwolf, M. Hohenstein, F. Phillipp, O. Brandt, G. E. Crook, and K. Ploog, "Direct measurement of local lattice distortions in strained layer structures by HREM," Ultramicroscopy **49**, 273–285 (1993).
[7]M. Hýtch, F. Houdellier, F. Hüe, and E. Snoeck, "Nanoscale holographic interferometry for strain measurements in electronic devices," Nature **453**, 1086–1089 (2008).
[8]C. T. Koch, V. B. Özdöl, and P. A. van Aken, "An efficient, simple, and precise way to map strain with nanometer resolution in semiconductor devices," Appl. Phys. Lett. **96**, 091901 (2010).
[9]A. Béché, J. L. Rouvière, J. P. Barnes, and D. Cooper, "Strain measurement at the nanoscale: Comparison between convergent beam electron diffraction, nano-beam electron diffraction, high resolution imaging and dark field electron holography," Ultramicroscopy **131**, 10–23 (2013).
[10]J.-L. Rouviere, A. Béché, Y. Martin, T. Denneulin, and D. Cooper, "Improved strain precision with high spatial resolution using nanobeam precession electron diffraction," Appl. Phys. Lett. **103**, 241913 (2013).
[11]M. P. Vigouroux, V. Delaye, N. Bernier, R. Cipro, D. Lafond, G. Audoit, T. Baron, J. L. Rouvière, M. Martin, B. Chenevier *et al.*, "Strain mapping at the nanoscale using precession electron diffraction in transmission electron microscope with off axis camera," Appl. Phys. Lett. **105**, 191906 (2014).
[12]C. Mahr, K. Müller-Caspary, T. Grieb, M. Schowalter, T. Mehrtens, F. F. Krause, D. Zillmann, and A. Rosenauer, "Theoretical study of precision and accuracy of strain analysis by nano-beam electron diffraction," Ultramicroscopy **158**, 38–48 (2015).
[13]T. C. Pekin, C. Gammer, J. Ciston, A. M. Minor, and C. Ophus, "Optimizing disk registration algorithms for nanobeam electron diffraction strain mapping," Ultramicroscopy **176**, 170–176 (2017).
[14]V. B. Ozdol, C. Gammer, X. G. Jin, P. Ercius, C. Ophus, J. Ciston, and A. M. Minor, "Strain mapping at nanometer resolution using advanced nanobeam electron diffraction," Appl. Phys. Lett. **106**, 253107 (2015).
[15]K. Müller, A. Rosenauer, M. Schowalter, J. Zweck, R. Fritz, and K. Volz, "Strain measurement in semiconductor heterostructures by scanning transmission electron microscopy," Microsc. Microanal. **18**, 995–1009 (2012).
[16]M. Simson, H. Ryll, H. Banba, R. Hartmann, M. Huth, S. Ihle, L. Jones, Y. Kondo, K. Muller, P. D. Nellist *et al.*, "4d-stem imaging with the PNCCD (s) tem-camera," Microsc. Microanal. **21**, 2211 (2015).
[17]H. F. Poulsen, J. A. Wert, J. Neuefeind, V. Honkimäki, and M. Daymond, "Measuring strain distributions in amorphous materials," Nat. Mater. **4**, 33–36 (2005).
[18]S. Scudino, B. Jerliu, S. Pauly, K. B. Surreddi, U. Kühn, and J. Eckert, "Ductile bulk metallic glasses produced through designed heterogeneities," Scr. Mater. **65**, 815–818 (2011).
[19]F. O. Méar, G. Vaughan, A. R. Yavari, and A. L. Greer, "Residual-stress distribution in shot-peened metallic-glass plate," Philos. Mag. Lett. **88**, 757–766 (2008).
[20]C. Ebner, R. Sarkar, J. Rajagopalan, and C. Rentenberger, "Local, atomic-level elastic strain measurements of metallic glass thin films by electron diffraction," Ultramicroscopy **165**, 51–58 (2016).
[21]C. Gammer, J. Kacher, C. Czarnik, O. L. Warren, J. Ciston, and A. M. Minor, "Local and transient nanoscale strain mapping during in situ deformation," Appl. Phys. Lett. **109**, 081906 (2016).
[22]C. Gammer, V. B. Ozdol, C. H. Liebscher, and A. M. Minor, "Diffraction contrast imaging using virtual apertures," Ultramicroscopy **155**, 1–10 (2015).
[23]M. J. Hart, R. Bassiri, K. B. Borisenko, M. Veron, E. F. Rauch, I. W. Martin, S. Rowan, M. M. Fejer, and I. Maclaren, "Medium range structural order in amorphous tantala spatially resolved with changes to atomic structure by thermal annealing," J. Non-Cryst. Solids **438**, 10–17 (2016).
[24]X. Mu, D. Wang, T. Feng, and C. Kübel, "Radial distribution function imaging by STEM diffraction: Phase mapping and analysis of heterogeneous nanostructured glasses," Ultramicroscopy **168**, 1–6 (2016).
[25]N. Mattern, J. Bednarčik, S. Pauly, G. Wang, J. Das, and J. Eckert, "Structural evolution of Cu-Zr metallic glasses under tension," Acta Mater. **57**, 4133–4139 (2009).
[26]C. A. Volkert, A. Donohue, and F. Spaepen, "Effect of sample size on deformation in amorphous metals," J. Appl. Phys. **103**, 083539 (2008).
[27]J. Ding, S. Patinet, M. L. Falk, Y. Cheng, and E. Ma, "Soft spots and their structural signature in a metallic glass," Proc. Natl. Acad. Sci. **111**, 14052–14056 (2014).
[28]P. Yu and H. Y. Bai, "Poisson's ratio and plasticity in CuZrAl bulk metallic glasses," Mater. Sci. Eng. A **485**, 1–4 (2008).
[29]L. Tian, Y.-Q. Cheng, Z.-W. Shan, J. Li, C.-C. Wang, X.-D. Han, J. Sun, and E. Ma, "Approaching the ideal elastic limit of metallic glasses," Nat. Commun. **3**, 609 (2012).
[30]M. Zhang, Y. M. Wang, F. X. Li, S. Q. Jiang, M. Z. Li, and L. Liu, "Mechanical relaxation-to-rejuvenation transition in a Zr-based bulk metallic glass," Sci. Rep. **7**, 625 (2017).
[31]H. S. Shahabi, S. Scudino, I. Kaban, M. Stoica, B. Escher, S. Menzel, G. B. M. Vaughan, U. Kühn, and J. Eckert, "Mapping of residual strains around a shear band in bulk metallic glass by nanobeam X-ray diffraction," Acta Mater. **111**, 187–193 (2016).
[32]S. Scudino, R. N. Shahid, B. Escher, M. Stoica, B. S. Li, and J. J. Kruzic, "Mapping the cyclic plastic zone to elucidate the mechanisms of crack tip deformation in bulk metallic glasses," Appl. Phys. Lett. **110**, 081903 (2017).
[33]D. R. G. Mitchell and J. A. Van den Berg, "Development of an ellipse fitting method with which to analyse selected area electron diffraction patterns," Ultramicroscopy **160**, 140–145 (2016).
[34]A. S. Argon, "Plastic deformation in metallic glasses," Acta Metall. **27**, 47–58 (1979).